SLAC–PUB–8682
November,2 2000

Results from the Beam Test of the Engineering Model of the GLAST Large Area Telescope *

E. do Couto e Silva,[1] P. Anthony,[1] R. Arnold,[2] H. Arrighi,[3] E. Bloom,[1] B. Baughman,[4] J. Bogart,[1] P. Bosted,[2] B. Bumala,[5] A. Chekhtman,[6] N. Cotton,[4] A. Crider,[7] I. Dobbs-Dixon,[4] A. Djannati–Atai,[6] R. Dubois,[1] D. Engovatov,[1] P. Espigat,[6] J.L. Evans,[1] T. Fieguth,[1] D. Flath,[1] M. Frigaard,[3] B. Giebels,[1] S. Gillespie,[8] G. Godfrey,[1] J.E. Grove,[7] T. Handa,[1] T. Hansl-Kozanecka,[9] J. Hernando,[4] M. Hicks,[1] M. Hirayama,[4] W.N. Johnson,[7] R. Johnson,[4] T. Kamae,[10] W. Kroeger,[4] D. Lauben,[5] Y.C. Lin,[5] T. Lindner,[1] P. Michelson,[5] A. Moiseev,[3] M. Nikolaou,[11] P. Nolan,[5] A. Odian,[1] T. Ohsugi,[10] J. Ormes,[3] G. Paliaga,[4] P. Saz Parkinson,[1] B. Phlips,[7] S. Ritz,[3] S. Rock,[2] J.J. Russel,[1] H. Sadrozinski,[4] T. Schalk,[4] J. Silvis,[3] Z. Szalata,[1] R. Terrier,[6] D.J. Thompson,[3] D.M. Tournear,[1] A.P. Waite,[1] J. Wallace,[5] S. Williams,[5] R. Williamson,[5] G. Winker.[4]

[1] *Stanford Linear Accelerator Center, 2575 Sand Hill Rd., Menlo Park, CA, 94025, USA*
[2] *University of Massachusetts, Amherst, MA, 01003, USA*
[3] *NASA/Goddard Space Flight Center, 8800 Greenbelt Road, Greenbelt, MD, 20771, USA*
[4] *SCIPP, University of California at Santa Cruz, Santa Cruz, CA 95064, USA*
[5] *Stanford University, Stanford, CA, 94305, USA*
[6] *PCC - College de France, 11, Place Marcelin Berthelot, 75231 Paris Cedex 05, France*
[7] *U.S. Naval Research Laboratory, 4555 Overlook Ave. S.W., Washington, DC 20375, USA*
[8] *University of Washington, Seattle, WA 98195, USA*
[9] *CEA, DSM/DAPNIA, Centre d'Etudes de Saclay, Gif-sur-Yvette, France*
[10] *Dept. of Physics, Hiroshima University, Higashi–Hiroshima, Hiroshima, Japan 739*
[11] *Royal Institute of Technology, Department of Physics, SE-100 44 Stockholm, Sweden*

Abstract

This paper describes the results of a beam test using the Engineering Model of the GLAST Large Area Telescope, which was installed in a beam of positrons, hadrons and tagged photons at SLAC. The performance of the four subsystems, Anti Coincidence Detector, Silicon Tracker, Calorimeter and Data Acquisition will be described.

*Work supported by Department of Energy contract DE–AC03–76SF00515 and NASA contract NAS5–98039.

1 Introduction

The principal objective of the GLAST mission involves the observation of energetic gamma rays, starting at about 20 MeV and extending as high as TeV energies [1]. The first all–sky survey above 50 MeV was performed by the CGRO–EGRET instrument [2]. The GLAST Large Area Telescope (LAT) will provide substantial overlap with ground–based gamma–ray telescopes to explore together a greatly expanded dynamic range compared to EGRET with well–matched capabilities. It will offer tremendous opportunities for discoveries in high–energy astrophysics with >50 times better sensitivity than EGRET. The GLAST LAT, is a pair–conversion telescope with modular design. Each of its 16 modules (towers) consists of a tracker/converter for direction measurement, followed by a calorimeter for energy measurement and surrounded by veto counters for cosmic–ray background rejection. The design employs modern and reliable technology commonly applied in particle physics experiments. Requirements such as reduced power consumption, self-triggering electronics and large effective area (>8000 cm^2) provide a new challenge for the science community in designing a simple, yet robust experiment, which can be built in relatively short time.

The technology choices and detailed simulations were verified in a beam test in 1997 [3]. The SLAC 1999/2000 beam test focuses on systems integration, data acquisition performance, validation of Monte Carlo simulations for on-axis and off-axis incident beams and studies with a hadron beam. For this test, the GLAST collaboration built the Beam Test Engineering Model (BTEM) whose overall size is close to that of one of the modules of the full GLAST instrument. Note that not all features of the flight design have been incorporated yet.

2 Beam Test Engineering Model (BTEM)

The BTEM tower is shown in Fig. 1. It consists of an Anti Coincidence Detector (ACD), a Calorimeter (CAL), a Silicon Tracker (TKR) and a Data Acquisition System (DAQ). The ACD design relies on segmentation to avoid the self–veto problem of EGRET [2] while still providing high cosmic-ray rejection. Self–veto events are caused by backsplash, secondary particles and photons produced in the shower of a high energy cascade in the calorimeter. The silicon tracker employs a design for photon conversions with passive material (Pb) interleaved between the silicon planes. While the front section is equipped with 11 thin (3.6% X_0) lead converters, the back section, close to the CsI calorimeter, contains 3 thick (28% X_0) lead converters. The front section is designed to ensure good measurement of the incoming photon direction whereas the back section ensures a better sensitivity to reduced fluxes at the expense of degraded angular resolution especially at lower energies. The total radiation length of the tracker including the support material amounts to 1.5 X_0. The CsI calorimeter is arranged in a hodoscopic configuration, in which each layer is rotated 90° with respect to its neighbors, forming an x-y array. This segmentation provides a valuable imaging capability for high-energy photons (E > 1 GeV) an plays an important role in the rejection of the background. The total radiation length of the calorimeter corresponds to 10 X_0, hence shower maxima up to ∼50 GeV are contained at normal incidence.

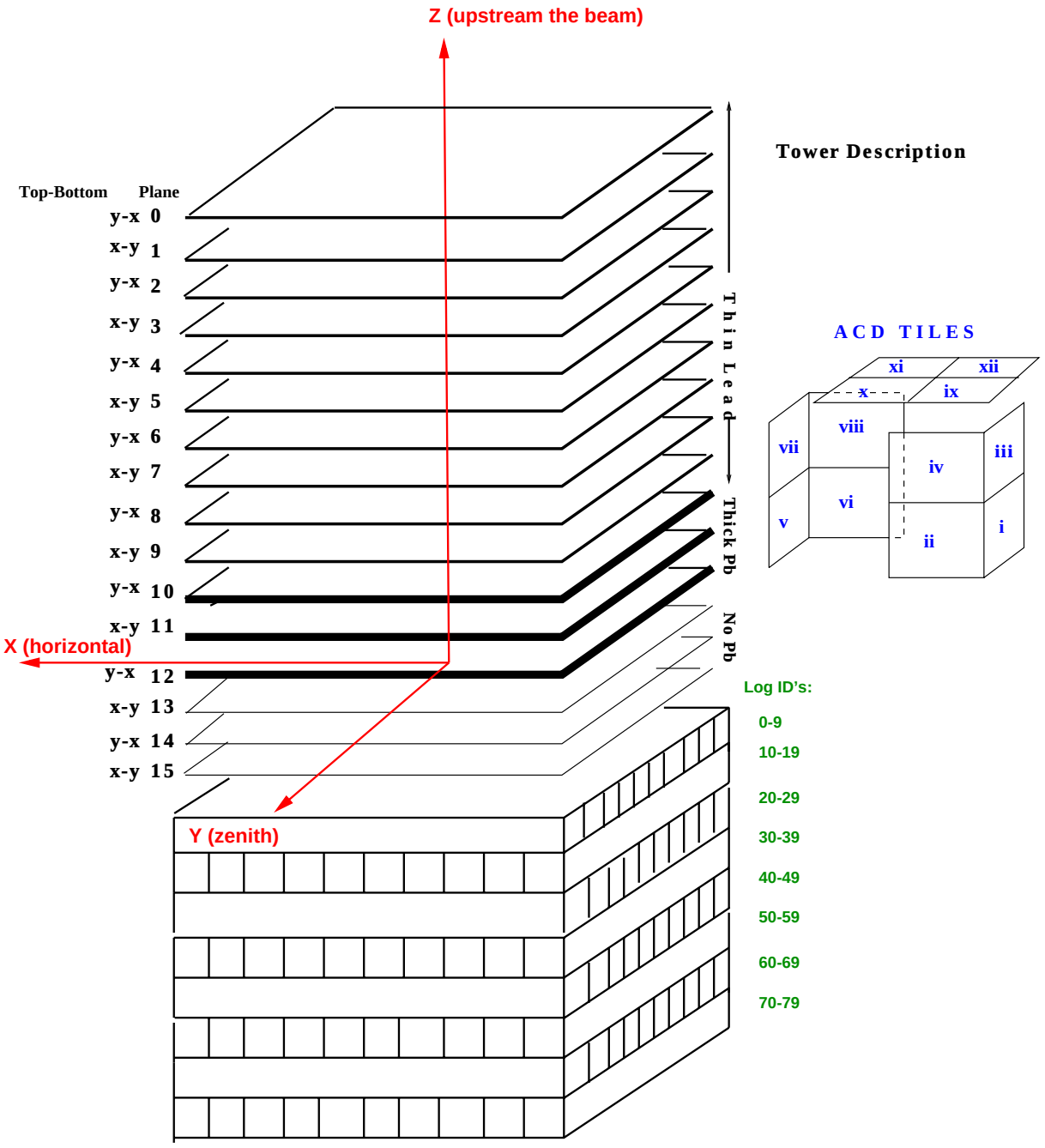

Figure 1: A schematic drawing (not to scale) of the Engineering Model (BTEM). The ACD tiles are arranged in a "hat" configuration to enclose the silicon tracker.

2.1 Anti Coincidence Detector (ACD)

The ACD consists of a "hat" that covers the tracker and is divided into 12 scintillating tiles (see Fig. 1). Light collected from the scintillators using wavelength–shifting–fibers, which are glued into grooves of the face of the scintillator. These fibers absorb, re–emit and deliver scintillator light to the photomultiplier tubes (PMT Hamamatsu R1635). The signals from the PMT are preamplified and delivered through coaxial cables to the ACD VME crate that contains front–end electronics boards. These were designed to serve as a prototype for the GLAST balloon flight (2001) without major modifications. These boards create the data formats containing a fast discriminator "veto" signal along with pulse height information and housekeeping data.

2.2 Silicon Tracker (TKR)

The silicon tracker has 41,600 readout channels. The electronics has been described elsewhere [4]. It employs a self–triggering binary readout scheme with sparsification. Detectors are singled–sided, high resistivity n type silicon with 194 μm readout pitch. Since the number of detectors purchased was not sufficient to fully instrument the tracker, the total silicon area corresponds to 81% (2.7 m^2) of the total area of one final LAT tower. This is the largest area of silicon tracker built to date. Details on the construction of the tracker and the quality of the detectors can be found in [5] and [6]. Fig 1 depicts the layout of the silicon tracker. There are 17 mechanical modules labeled trays. Each tray consists of 2 layers of detectors whose strips are oriented along the same direction. In between both layers in the same tray, near the bottom, one finds lead converters. Trays with strips along x and y directions alternate throughout the tracker. The top and bottom layers of the tracker are not instrumented with silicon detectors. Since the first level trigger requires 3 hits in a row for each of the spatial projections (x and y), the bottom three trays are not equipped with lead converters. Therefore, a total of 32 layers (16 planes) are read out by the electronic boards mounted on the sides of the trays.

2.3 Calorimeter (CAL)

There are in total 80 thallium–doped CsI scintillation crystals with dimensions of 3.0 cm $\times$ 2.3 cm $\times$ 31 cm arranged in a hodoscopic configuration. As shown in Fig. 1, there are 8 layers of 10 crystals. Each layer is rotated 90° with respect to its neighbors, forming an x-y array. The crystals are read out by 2 PIN photodiodes at each of their ends that measure the scintillation light from an energy deposition in the crystal that is transmitted to each end. The active areas of the two diodes have a ratio of 4:1. Their spectral response is well matched to the scintillation spectrum of CsI(Tl), which provides a large primary signal ($\simeq$3,000 electrons collected in 1 cm^2 diode per MeV deposited), with correspondingly small statistical fluctuations and thereby high intrinsic spectral resolution. Photodiodes have relatively low operating voltages ($\simeq$ 50 V), which simplifies their use in space relative to photomultiplier tubes. To avoid saturation at high energies the dynamic range of 5 $\times$ 10^5 is divided into two independent signal chains, the low energy (2 to 800 MeV) and the

high energy (40 MeV to 100 GeV). There are also two gains, so that from 2 MeV up to 100 GeV one has four ranges that overlap. The significant overlap between the two ranges allows cross–calibration of the electronics. The difference in light levels at each end of a log provides a determination of the position of the energy deposition along the CsI crystal. The position resolution of this imaging method ranges from a few millimeters for low energy depositions ($\simeq$10 MeV, see [3]) to a fraction of a millimeter for large energy depositions (>1 GeV). The low power consumption per CsI crystal required the development of a custom CMOS ASIC that is optimized to the performance requirements of the GLAST calorimeter.

2.4 Data Acquisition System (DAQ)

The DAQ consists of four Tower Electronics Modules (TEMs). These are VME cards that interface to the instruments: tracker (TKR), calorimeter (CAL), and anti–coincidence detector (ACD). The primary role of the TEMs was to accept trigger request primitives from one or more instrument front-end(s) or external source, generate and distribute a global Level-1 trigger (L1t) to all the instruments for each event, and then read out and buffer the event data until collected by the local CPUs. Each TEM had its own 20 MHz system clock to drive the on-board logic and provided a high-resolution time-stamp for each event data fragment. A fourth TEM was used as a "spacecraft interface unit" (SIU) which collected GPS time and tower fixture x-y-θ orientation, plus beamline, time-of-flight, neutron detector and photon tagger data from the end-station electronics for subsequent data analysis.

3 Particle Beams and Neutron Counters

Figure 2 displays the experimental set–up for the particle beams and the experiment.

3.1 Charged Particles and Particle Identification

A secondary beam of positrons was created by allowing the primary electron beam (30 GeV) of bunch intensity of 3.5×10^{10} from the SLAC LINAC to impinge on a target. Positrons were created in the radiator in a two–step process of bremsstrahlung followed by pair creation. A magnet swept the initial and pair created electrons into a dump, while positrons were bent in the opposite direction through a collimator and a magnetic analysis system to provide a beam of variable energy positrons in the experimental hall. The mean number of positrons per bunch could be varied from 0 to 100. The size of the bunch in all three dimensions is of the order of a few millimeters except at the lowest energy.

The BTEM's response to positrons was determined using a beam of about 0.8 positrons per bunch with a repetition rate of 30 Hertz and momentum resolution of the order of 1%. Positron beam energies of 20, 5, and 1.6 GeV were employed. To simulate the calorimeter's response to high-energy depositions, a beam of up to 50 positrons per pulse at 20 GeV was sent into the BTEM. This tested the linearity by noting the pulse height peaks for a varying number of positrons.

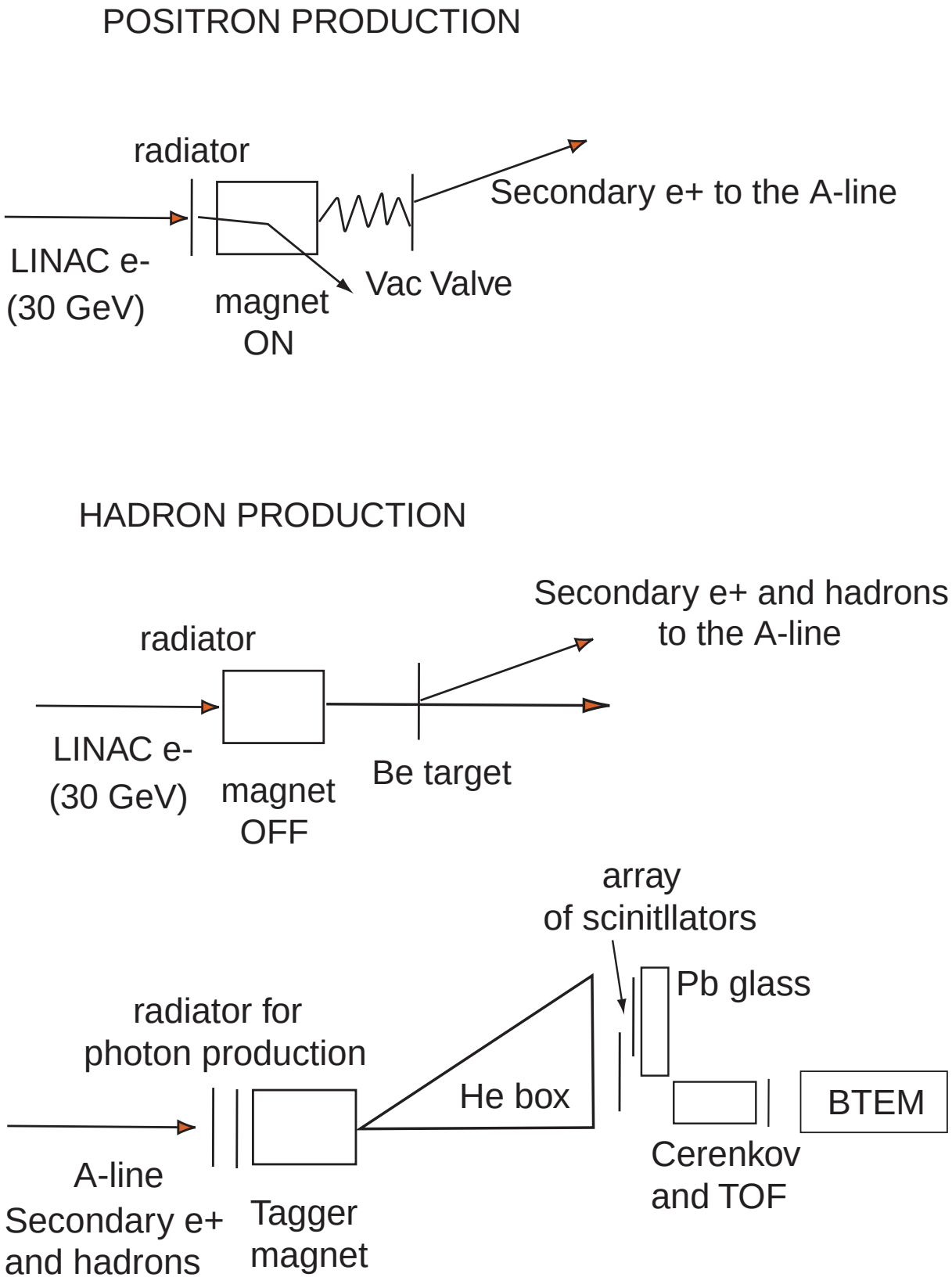

Figure 2: A schematic drawing (not to scale) of the experimental set–up.

A Beryllium target in the LINAC electron beam was the source of the "hadron" beam. The magnet that previously sent the positrons produced at 0° degrees into the collimator and magnetic analysis system was shut off. The collimator then accepted particles produced at 0.5° to the incident electron beam reducing the number of positrons relative to pions and protons, such that about 50% of the particles accepted into the A–line were positrons, ∼50% pions, 0.4% protons and ≤ 1% kaons for a beam momentum of 13 GeV/c. A gas Cerenkov counter separated positrons and pions from kaons and protons. A time of flight system separated the protons from the kaons. The beam intensity was maintained a little below 1 particle per pulse.

3.2 Tagged Photons

A tagged photon beam tested the prototype's response to photons of various energies. This beam used the positron beam hitting various radiators from 0.9% to 8.9% radiation lengths. A magnet then deflected the positrons into the tagging system. This tagging system measured the energy of the positrons degraded by bremsstrahlung in the radiator. The photon energy was therefore tagged as the difference between the incident and outgoing positron energies. The energy of the outgoing positron was measured by its deflection after traversing the magnetic field. A picket array of tagging scintillators backed up by lead glass counters determined the positron energy. The intensity was about one tag per pulse.

The tagger magnet has a dipole field that was adjustable to 21 kG. The deflection angle (in radians) of the primary beam was 1.24/E(GeV) for E > 7 GeV, and was fixed to 0.1 radians for E < 7 GeV by choosing the corresponding lower field strength. The hodoscope for tagging was located about 7.5 m downstream from the center of the magnet, covering the distances traverse to the beam from 0.4 to 2.9 m. There were two arrays of hodoscope fingers, each 3 cm wide, which overlap to provide a 1 cm granularity corresponding to 3 mm *rms* resolution. These arrays were followed by 17 lead glass blocks with a front surface area of 14.2 by 14.2 cm^2 and a length of 42 cm. The energy resolution was $8\%/\sqrt{E(\mathrm{GeV})}$.

3.3 Neutron Counters

Low energy neutrons produced in the CsI calorimeter can interact in the hydrogen within the plastic scintillator of the ACD to give an additional self veto mechanism for GLAST besides backsplash photons. To measure the neutron contribution, three scintillators were installed above the CsI calorimeter (see Fig. 3). Two scintillators consisted of Bicron 408 plastic scintillators 1 and 2 cm thick. The third scintillator was a 3 mm–thick NaI. Each consisted of a 3 inch photomultiplier directly coupled to a 3 inch diameter scintillator. Scintillators were mounted 47 cm from the tower axis and midway between the front and the rear of the calorimeter faces. Neutrons and low energy photons are expected to count in the two hydrogen rich plastic scintillation counters, while primarily photons should count in the NaI.

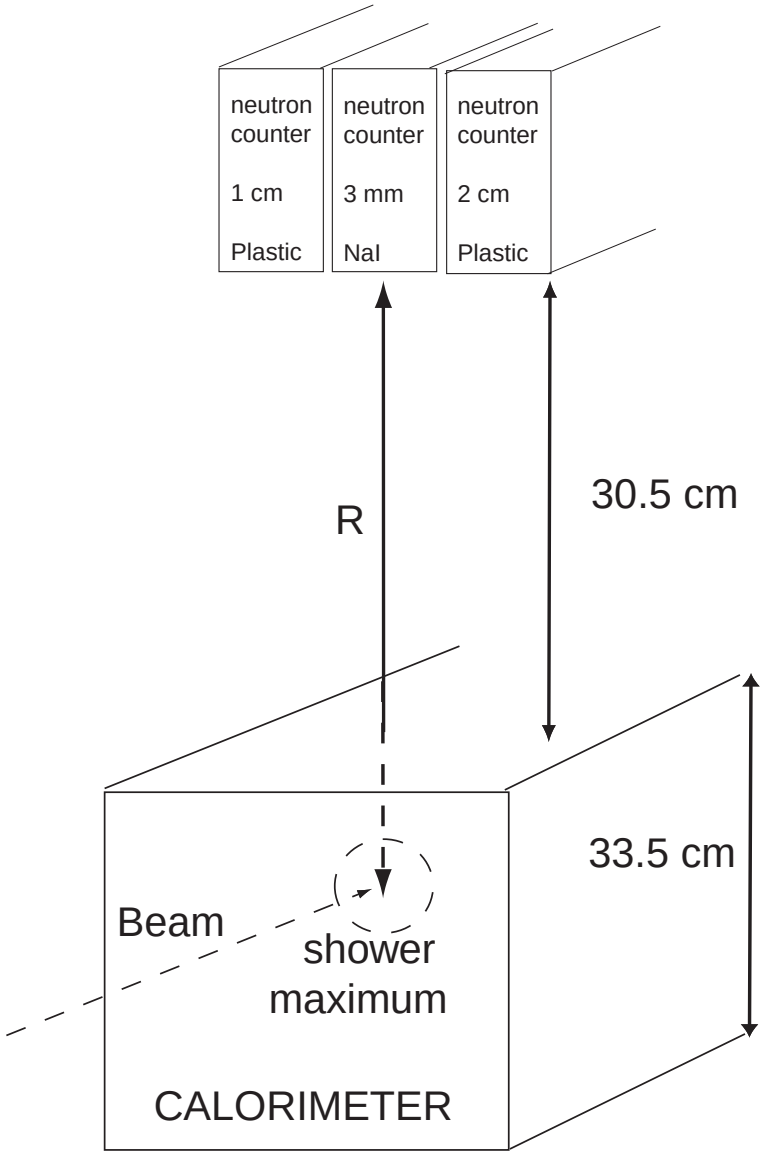

Figure 3: Schematic drawing (not to scale) of the location of the neutron counters with respect to the calorimeter.

4 Trigger and Data Acquisition

4.1 Trigger

The BTEM DAQ global Level-1 trigger circuit accepts trigger–request input primitives from the tracker, the calorimeter and the ACD, as well as from a general external trigger input. It distributes the resulting fast–OR Level–1 trigger signal to all instrument sub–system front–ends via redundant, fault–tolerance hardware lines. In addition the Level–1 trigger circuit monitors deadtime and deadtime cause from each sub-system and also the Tracker front–end buffer occupancy in order to determine whether a given trigger–request can be honored. Thus all sub–systems were always read out together.

For most runs, the accelerator beam pulse triggered the BTEM, and the states of the Level–1 trigger were recorded. This allowed an unbiased verification of the trigger system. For limited runs, the BTEM was also operated in a variety of true self–trigger modes (with the beam trigger disabled). The self trigger for the silicon tracker was configured as a logical AND of hits in three consecutive layers for each of the two measured coordinates (x and y). The calorimeter self trigger was based on low level discriminators. The ACD TEM was set up to generate *vetoes* rather than triggers, generated by the ACD's low level discriminators. These signals also could veto the tracker and/or the CAL by hardware means, preventing these detectors from responding to events due to charged particles. There was good coincidence margin (>300 ns) between the latest ACD veto outputs and the earliest tracker and calorimeter outputs allowing veto of L1Ts to successfully occur. Both the ACD and calorimeter also have high level discriminators to detect events with Carbon, Nitrogen and Oxygen (CNO), but these were not used for the beam test.

The event timer in each TEM runs off of the clock source. When the event is captured, the 32-bit count value from this timer is captured and becomes part of the data set. As each event is assembled, the GPS time from the SIU is associated with the counter values from the TEMs, creating an absolute time for each event. In addition, it is possible to track the clock drift between TEMs by examining the timer data event–by–event and comparing over time as a function temperature. The BTEM deadtime time was $\simeq 60$ μs, limited by the calorimeter readout.

4.2 Data Acquisition

Each TEM provided a trigger count and fast timer stamp added on top of each subsystem data fragment as data were read from the instrument front-ends and placed in FIFO memory local to each VME crate which was sized to hold several hundred events if needed. Each event trigger also generated an interrupt for each local CPU to read the pending event data from the FIFO memory and forward the data over local Ethernet to a dedicated Sun workstation which collected and archived the data to local disks. Meanwhile the photon tagger data was collected using the standard CAMAC and VME hardware, and then also sent to the Sun workstation on an event–by–event basis as a fourth data stream, which was combined in real–time with the BTEM data by the Sun workstation. The Sun workstation provided basic run–control and minimal monitoring of the data streams to assess basic data integrity during

each run. Afterwards the raw data from each run was verified on an event–by–event basis to ensure event alignment using a both the high–resolution timers and the simultaneous energy measurements provided by the calorimeter and photon tagger, in preparation for conversion to the ROOT [7] and the HBOOK [8] data formats used by the offline analysis.

5 Data Analyses

5.1 Anti Coincidence Detector (ACD)

The ACD response to the amount of deposited energy was tested by selecting events with 1, 2 or 3 particles hitting the instrument simultaneously, using the calorimeter data. Figure 4a correlates the pulse height in the ACD with those from the calorimeter after pedestal subtraction. The three clusters from left to right correspond to 1, 2 and 3 particle events, respectively. Figures 4b, 4c and 4d depict the ACD pulse height distributions for 1, 2 and 3 particle events, respectively.

Assuming that the width of the distribution ($\epsilon = \Delta E/E$) is caused by the fluctuation on the mean number of photoelectrons created in a PMT photocathode in each particular event, we can estimate this number as $N_p = 1/\epsilon^2$. This simple analysis demonstrates the expected relationship between the energy deposited and the mean number of photoelectrons agrees well with data. The mean number of photoelectrons obtained from Fig 4b also agrees with that measured in the laboratory with cosmic rays. Assuming a Poisson pulse height distribution, this would meet the required efficiency of 0.9997 with 0.25 mip threshold. Note that the efficiency of the ACD to minimum ionizing particles (mips) has also been measured in the previous test beam [3] and in the laboratory. The self–veto caused by backsplash has been studied before over the energy range from 5 GeV to 300 GeV [3, 9].Data on backsplash obtained in this experiment agree with previous measurements.

5.2 Neutron Counters

The time and amplitude of the pulses were recorded relative to the arrival of the incoming beam. The pulse height conversion to energy was calibrated by using the 0.511 MeV gamma line from Na^{22}. The time difference between photons and 1 MeV neutrons depends on the neutron kinetic energy and the distance it must travel to the scintillator. Unfortunately, the NaI did not provide good enough time resolution for a time of flight measurement.

The energy of photons at the peak of an electromagnetic shower is around that of the critical energy, which for CsI is 12 MeV. This energy also is about equal to the energy of the Giant Dipole Resonance in heavy nuclei. A photon absorbed by this resonance results mainly in the ejection of a low energy ($\simeq$1 MeV) neutron. This effect is well known by radiation protection physicists designing shielding for electron linear accelerators. They use a crude rule of thumb, which states that for each GeV of electromagnetic energy deposited in matter a 0.2 MeV neutron is produced [10]. Combining the Giant Dipole Resonance production with the high cross section of low energy neutrons in the hydrogen within the

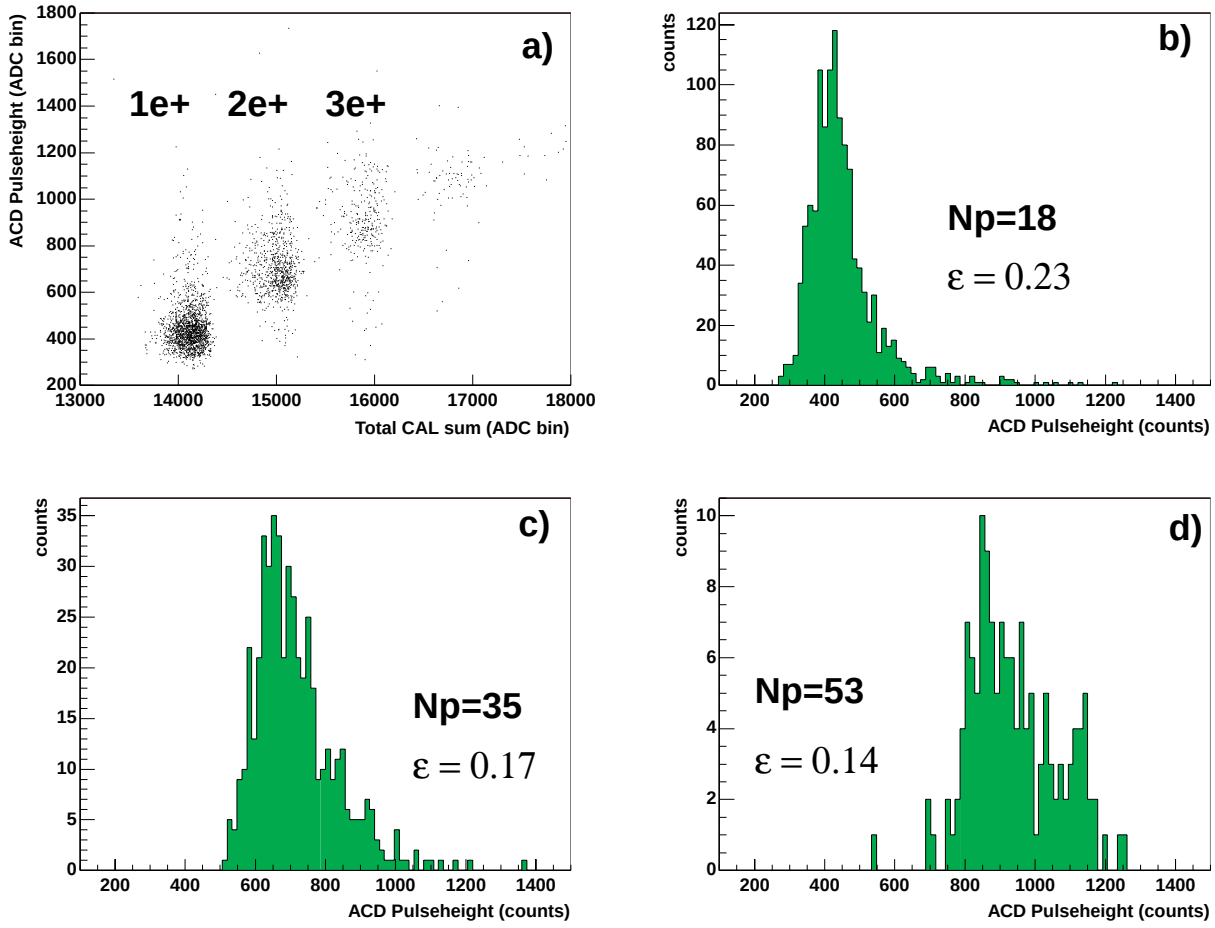

Figure 4: Correlation of pulse heights from the ACD and from the calorimeter after pedestal subtraction. a) The three clusters from left to right correspond to 1, 2 and 3 particle events, respectively; b), c), d) ACD pulse heights for 1, 2 and 3 particle events, respectively. The relative energy resolution is given by ϵ and N_p is the mean number of corresponding photoelectrons.

plastic scintillator of the ACD, gives an additional self veto mechanism for GLAST besides backsplash photons.

The radiated photons from a 20 GeV/c positron beam and 8.9% radiator were allowed to hit the CsI at a transverse distance of 54 cm from the 2 cm plastic scintillator. Figure 5 shows the pulse height versus time delay of the scintillator. There is a dense band due to prompt photons and few delayed events. The prompt peak (photons) is delayed for small pulses due to discriminator walk. The solid line corresponds the theoretical kinetic energy of a neutron as a function of its time of flight. A proton in the scintillator will recoil with this energy or less. The 15 data points that are not part of the prompt band correspond to the neutron candidates. Most of the events with pulse height above the discriminator threshold that would register as veto from backsplash are photons. However, most of the photons in Fig. 5 will be below the in-flight ACD discriminator threshold (400 keV). If the delayed events are assumed to be neutrons, the ratio of neutrons to photons is 0.09 ± 0.04 above 400 keV. There are 0.029 ± 0.008 neutron hits in a 4π solid angle $\times$ 2 cm thick plastic scintillator per GeV of energy deposited in the CsI. Since 0.33 of 1 MeV neutrons interact with the hydrogen in 2 cm of plastic scintillator, there were 0.09 ± 0.02 neutrons per GeV produced in the CsI. This is a factor of two smaller than the 0.2 neutrons/GeV estimate from the rule of thumb.

In order to gain confidence that the delayed events were neutrons from electromagnetic showers and not from charged pions interacting in the CsI, we selected beam pulses with only electromagnetic shower energy in the CsI. To this end, we used a hadron beam with momentum of 13.5 GeV/c and required two positrons per event. Figure 6 shows the number of scintillator hits in the 2 cm plastic scintillator versus the distance (R) from the location of the expected shower maximum in the CsI calorimeter. While hits from photon candidates (open squares) fall faster due to absorption in the CsI, those from neutron candidates (filled circles) decrease consistent with $1/R^2$ (solid line). From Fig 6 we estimate 0.033 ± 0.006 neutron hits in a 4πsolid angle $\times$ 2 cm thick plastic scintillator per GeV of energy deposited in the CsI, where the errors are only statistical. This is consistent with the results from Fig 5. and corresponds to less than 0.2 neutrons/GeV. Therefore neutrons do not contribute significantly as a source of backsplash.

5.3 Calorimeter (CAL)

5.3.1 Dynamic Range

One of the primary goals for the calorimeter at this beam test was to demonstrate a readout system with a very large dynamic range. To test this, a beam of 20 GeV positrons was incident on the calorimeter with the average beam intensity varied between $\sim$15 and $\sim$30 positrons per beam pulse. Figures 7 shows the total energy measured in the calorimeter in each of two gain ranges. Figure 7b corresponds to the lowest gain, highest energy range where individual peaks represent the variations in the number of positrons received in the beam pulses. In this run, the calorimeter was self–triggering with a discriminator threshold that was sensitive to cosmic ray muons. In Figures 7a, the highest gain and lowest energy range, the total energy deposition of individual muon tracks is evident. The width of the

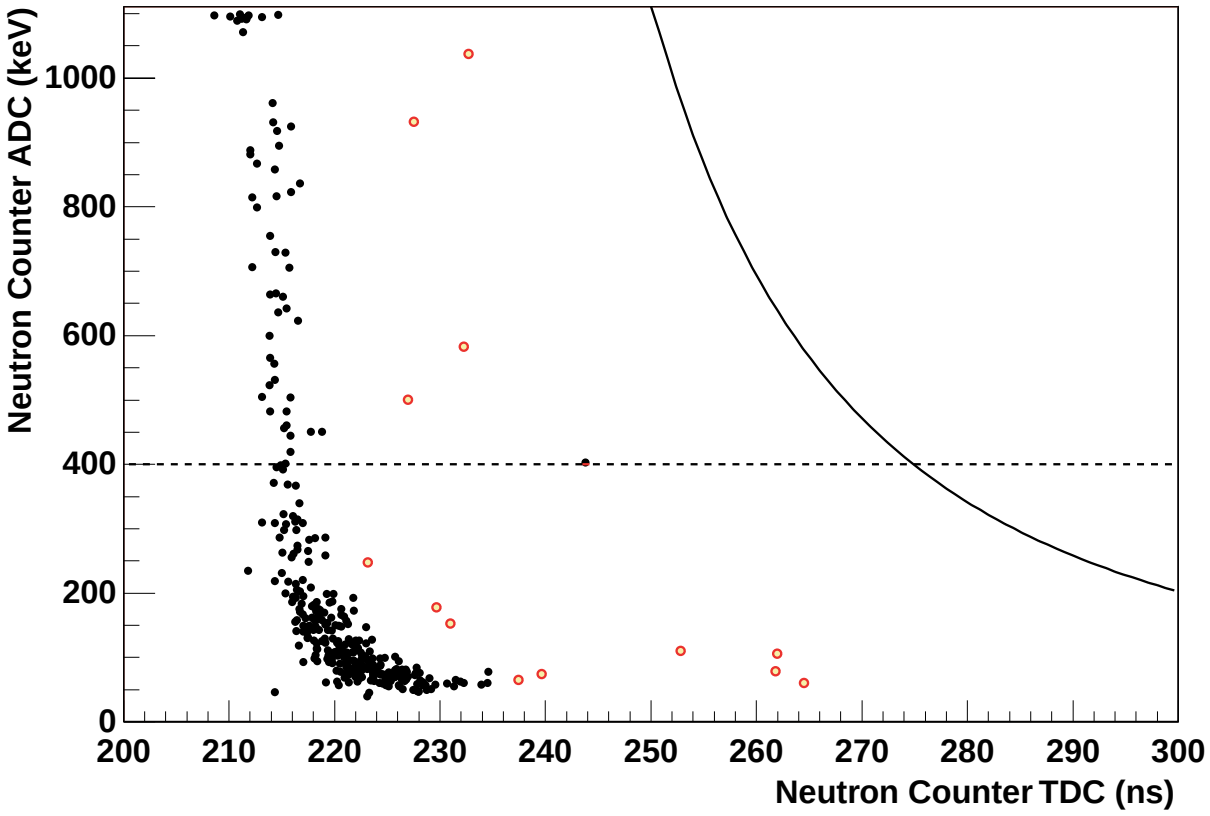

Figure 5: Pulse height versus the time delay measured by the 2 cm thick plastic scintillator for a photon run using an 8.9% radiator in the beam line. The solid line corresponds the theoretical kinetic energy of a neutron as a function of its time of flight. The 15 data points which are not part of the prompt band are the neutron candidates and the dashed line corresponds to the value for the ACD discriminator threshold.

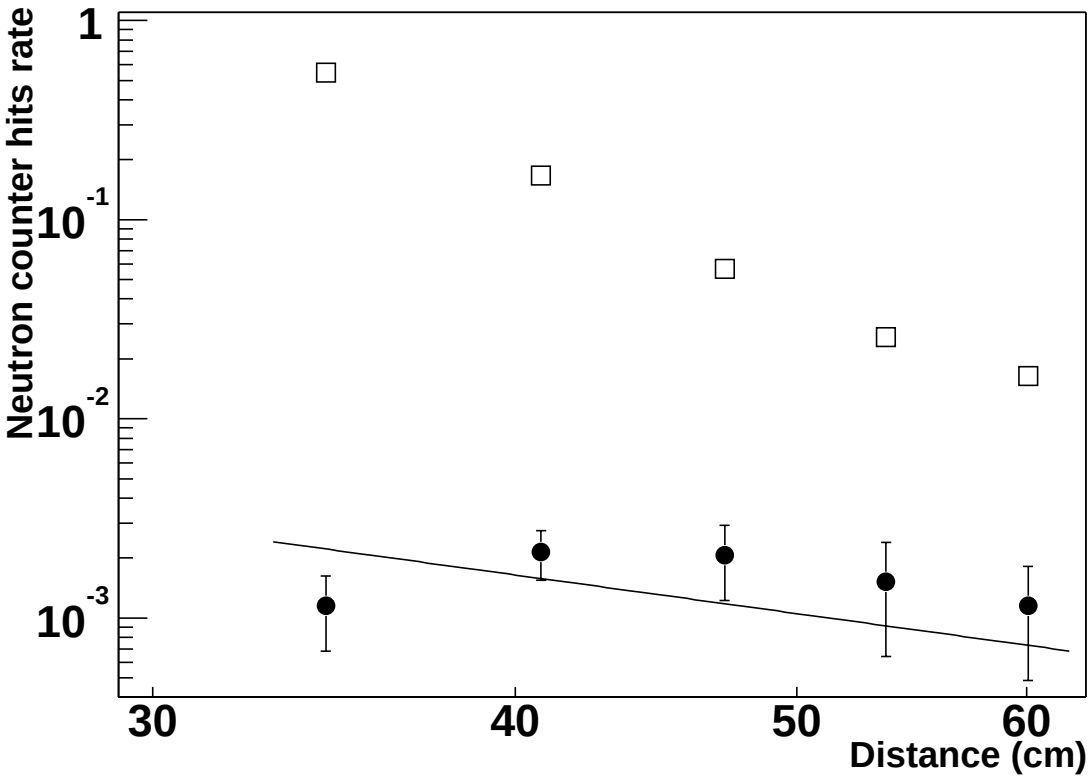

Figure 6: Number of scintillator hits in the 2 cm plastic scintillator versus the distance from the location of the expected shower maximum in the CsI calorimeter. Neutron candidates are represent by filled circles and photon by open squares. The $1/R^2$ dependence is depicted by the solid line.

muon peak is due to the variation in muon pathlengths through the calorimeter and is not indicative of the energy resolution of the calorimeter.

5.3.2 Energy Resolution

Because the calorimeter is 10 radiation lengths deep, the shower maximum is contained up to ~50 GeV at normal incidence. However, above a few GeV, a large amount of energy leaks out the back of the calorimeter, and the total energy measured is systematically less than the incident energy. We have employed two techniques to correct for the shower leakage.

The first involves fitting the profile of the captured energy to an energy–dependent, analytic description of the mean longitudinal shower profile. This profile is reasonably well described by a gamma distribution that is a function only of the location of the shower starting point and the incident energy. We used this technique in analysis of data from the 1997 beam test of the GLAST calorimeter [3].

The second method uses the correlation between the escaping energy and the energy deposited in the last layer of the calorimeter. Indeed, the last layer carries the most important information concerning the leaking energy: the total number of particles escaping through the back should be nearly proportional to the energy deposited in the last layer. The measured signal in that layer can therefore be modified to account for the leaking energy. We used the Monte Carlo simulation of the GLAST beam test configuration to determine this correlation at several energies, from 2 GeV up to 40 GeV. This simulation is based on the *GISMO* toolkit [11], which employs the *EGS4* electromagnetic shower code [12]. Minor modifications were necessary for the different geometry and readout used in the BTEM. These simulations show that at a given incident energy, the two–dimensional distribution of the energy escaping and the energy deposited in the last layer can be approximated by a simple linear function

$$E_{leak} = \alpha \cdot E_{last} + \beta, \tag{1}$$

where the empirically derived parameters α and β are proportional to the logarithm of the incident energy and to its square, respectively. Because the only information we have, initially, on the incident energy is the total energy deposited in all layers E_m, we have to use it as the estimator of E_0. The reconstructed energy is then

$$E_{rec} = E_m + \alpha(E_m) \cdot E_{last} + \beta(E_m) \tag{2}$$

To improve the result, one can iterate using the new estimator to determine the correct values of α and β.

Figure 8 shows the raw and reconstructed energy for 20 GeV incident positrons. The resolution of the raw distribution is about 7% (rms of the equivalent central Gaussian), while the reconstructed resolution is less than 4% by the correlation method and about 5% by profile fitting. There is a small bias (3%) due to the uncertainty in the gain calibration for the last layer. The reconstruction method applied to Monte Carlo simulated data yields an energy resolution of 3%, suggesting that some uncertainties remain in our calibration of beam test data.

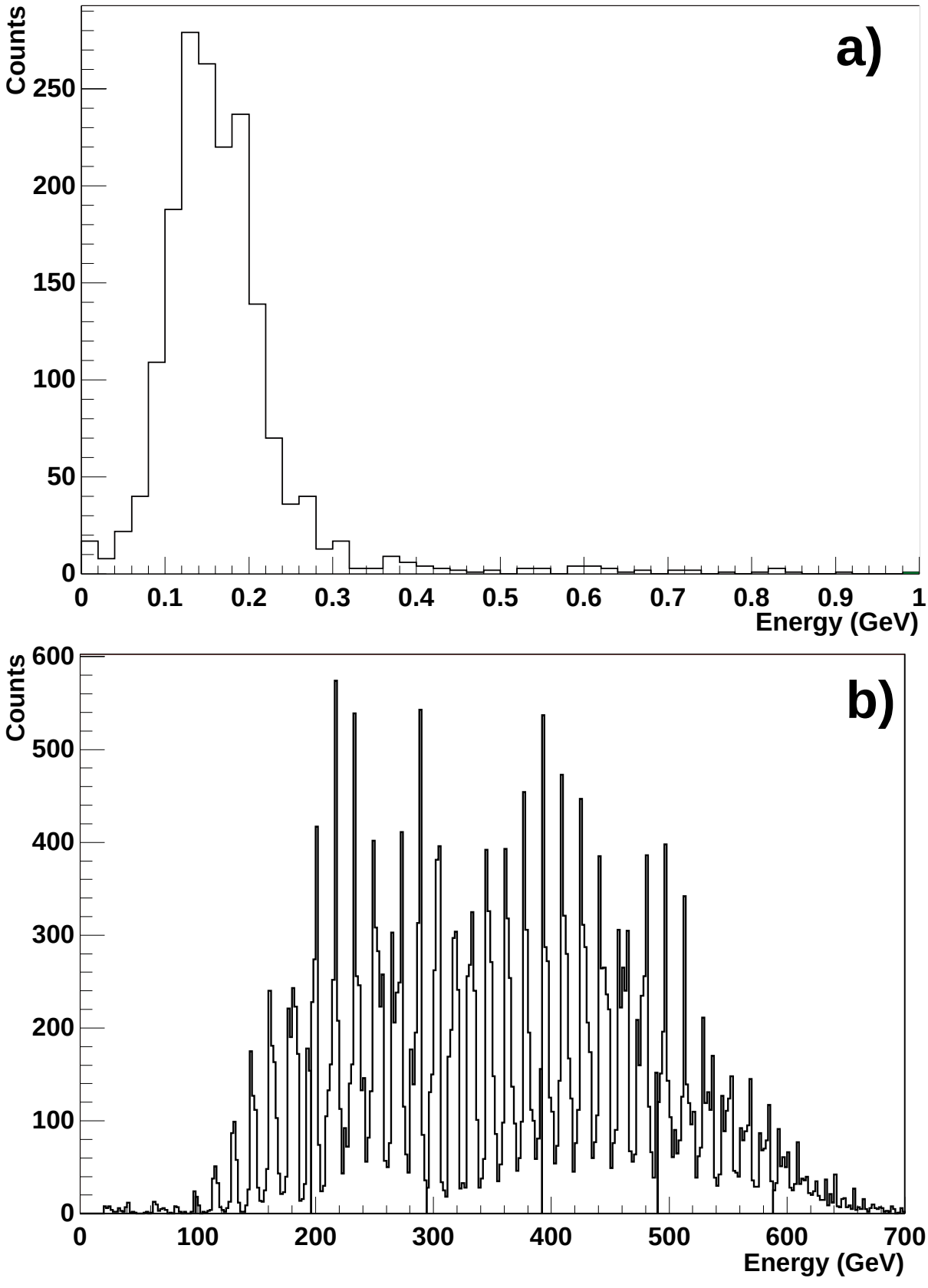

Figure 7: The total energy deposition in the calorimeter during a self–trigger test with the beam intensity varied between ∼15 and ∼30 positrons per pulse. Muon response is seen for a) the lowest energy range and for b) multi-positron response for the highest energy range.

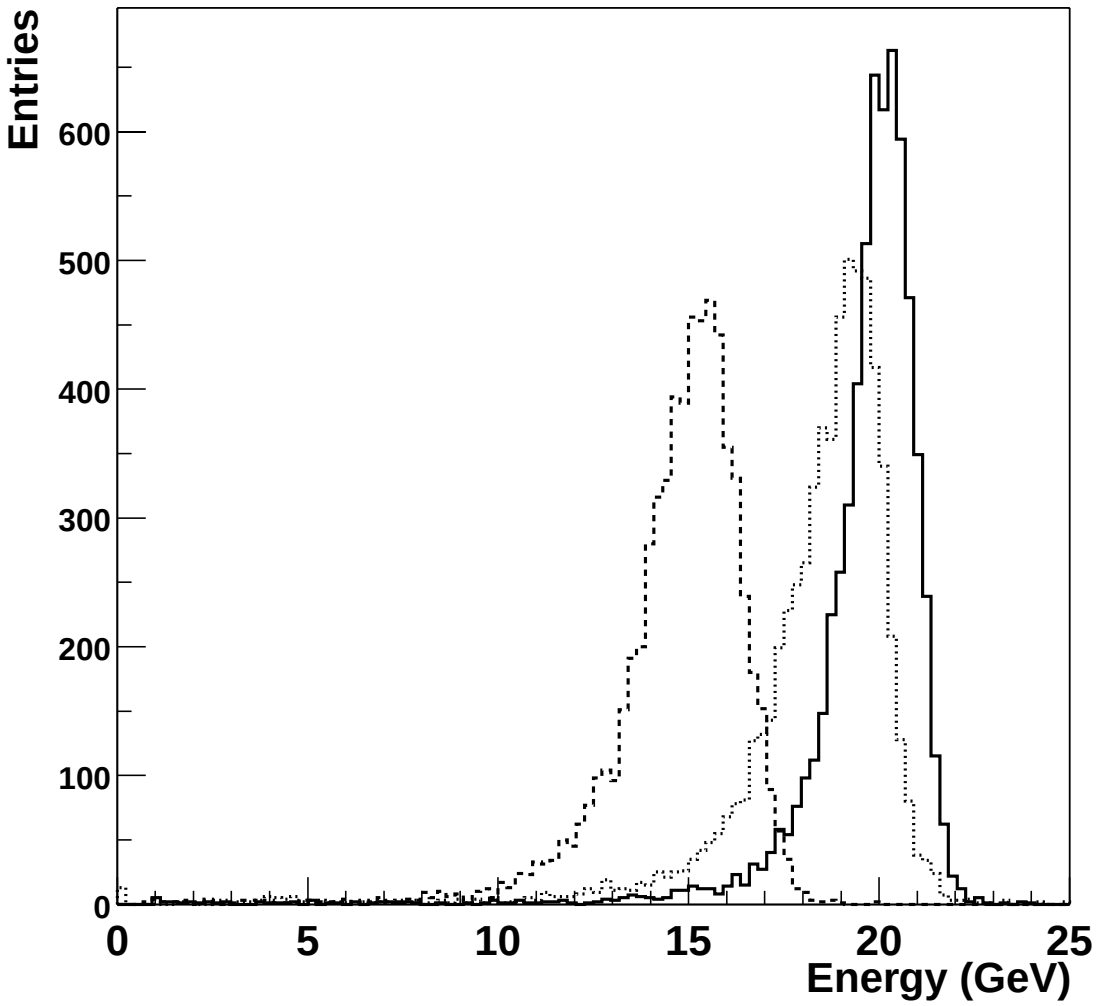

Figure 8: Sum of the energy of all crystals (dashed histogram), profile fitting (dotted histogram) and new correlation method (solid histogram) for 20 GeV incident positrons.

5.4 Silicon Tracker (TKR)

In this section we describe the studies on hit multiplicity, the alignment of the tracker, and a novel technique to locate conversion points using the Time–Over–Threshold and measurements of the point spread function.

5.4.1 Hit multiplicity

We compared the hit multiplicity distribution in a silicon tracker layer from the *GLASTSIM* Monte Carlo simulator and the beam test data. The stepping technique used by *GISMO* defines volumes by boundary representations, that is, it defines a set of intersecting surfaces, and extrapolates along particle trajectories by finding the distance to the nearest surface. Therefore thin layers of material, such as 400 μm of silicon, are correctly simulated. One of the parameters related to the energy transport in *EGS4* was adjusted to fit the beam test data. The cutoff energy in the *EGS4* was lowered from our default value of 500 keV to 100 keV, which is close to the most probable deposit energy of minimum ionizing particles in 400 μm thickness silicon detectors ($\simeq$ 40 keV). Particles with energy below the cutoff energy stop and deposit all their energy, thereby halting track propagation. Since the charge sharing between the neighboring strips is not included in *GLASTSIM*, it was estimated by comparing the ratio of double[†] to single hits using single–track hadron events. The effect was only $\simeq$10%.

The calorimeter energy was used to select 5 GeV single positron events in which noisy channels had a hit occupancy $> 0.1\%$ are removed. Note that these correspond to 25 out of 41,600 channels. Typical occupancies are the order of 10^{-5}. Figure 9 shows the hit multiplicity distributions for the two different planes at two incident beam angles, 0° and 30°. Plane 9 is located in the front section of the tracker (thin Pb converter) and plane 13 at the back section of the tracker (thick Pb converter). As expected, the layer right below the thick converter (Plane 13 layer x) shows higher hit multiplicity. The hit multiplicity was constrained by the readout system, which allows a maximum of 64 hits per layer. The hit multiplicity at 30° incidence for the same layer is smaller than that at 0°. This is explained by the fact that the beam at normal incidence goes through a larger number of layers. Figure 10 shows the mean value of the hit multiplicity for all layers. The steep increase of the multiplicity is from the presence of thick converter layers. For both angles there was good agreement between data and simulation.

5.4.2 Alignment

The mechanical survey of the silicon tracker indicated that strips were aligned in a plane better than 50 μm [5]. To verify that, the alignment with tracks was done using the hadron beam. Track reconstruction employed the Kalman filter method [14]. The Kalman filter optimizes the interplay between multiple scattering and position resolution as tracks propagate through the detector. Hadron beam runs distributed over the front face of the detector,

[†]Double hits are defined as a hit cluster consisting of two neighboring hit strips.

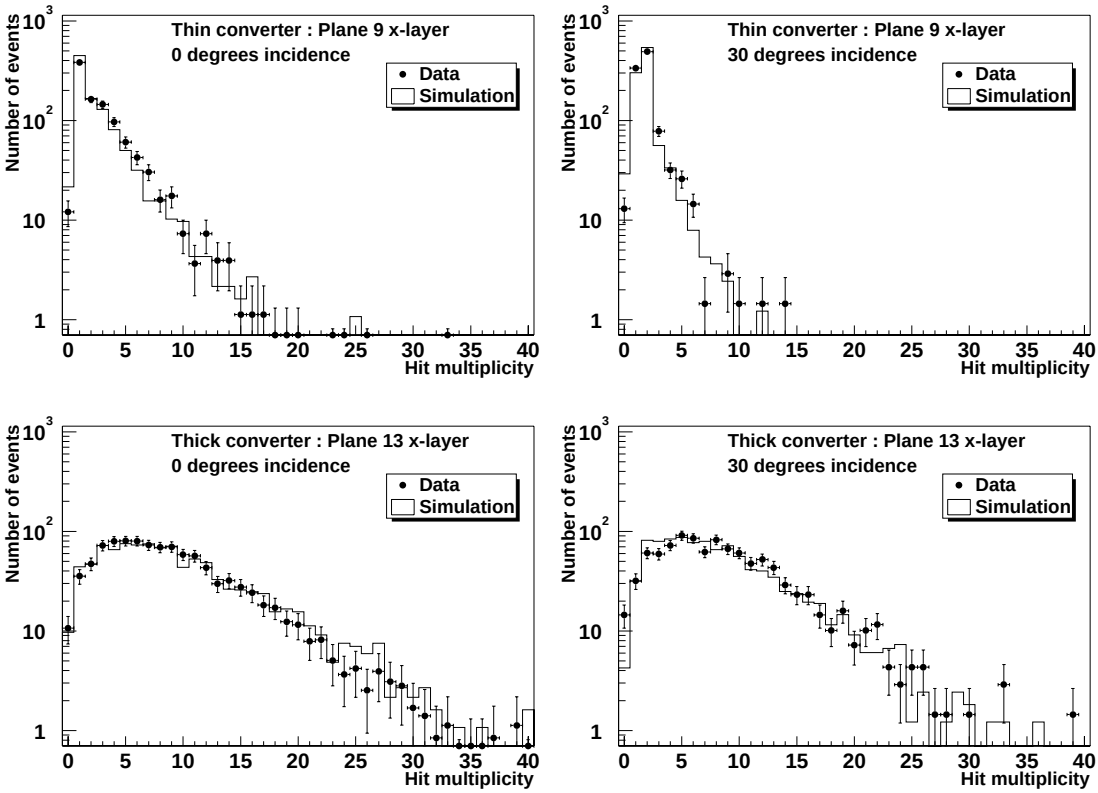

Figure 9: Mean hit multiplicity in the silicon tracker for 0° and 30° incidence with charge sharing correction applied to the *GLASTSIM* output. For the 30° data, the beam impinges on the side of the tracker at 30 cm below the top surface, for 0° it penetrates all layers.

at normal incidence and with incident momentum of 13.5 GeV/c were used for the alignment. The were two alignment methods used in this analysis: a two layer method and a least squares method. The two–layer method was the first process utilized in aligning the detector. After checking every possible track defined by any two hits in the entire detector, the track with the highest number of associated clusters was selected and defined as the best–track. If there were multiple tracks with the same number of clusters, the one with the lowest value of chi-squared was chosen. Clusters inconsistent to belonging to a track were removed. After the best track was found, a new track was created using a coordinate system defined by two fixed layers. The two points needed to define the new track were determined by the positions of the two clusters (associated with the best track) found on layers 8 and 15. Once this second track was established, it was possible to calculate the predicted positions of a cluster on any given layer or ladder. The residual of a given cluster is the difference between its predicted position and its measured position. Residuals were fit to a Gaussian and its mean determined the total offset.

The second phase of the process utilized the least squares method. The initial stages of the least squares method were exactly the same as those utilized in the two–layer method. An initial best–track was determined by finding the track, defined by any two hits in the

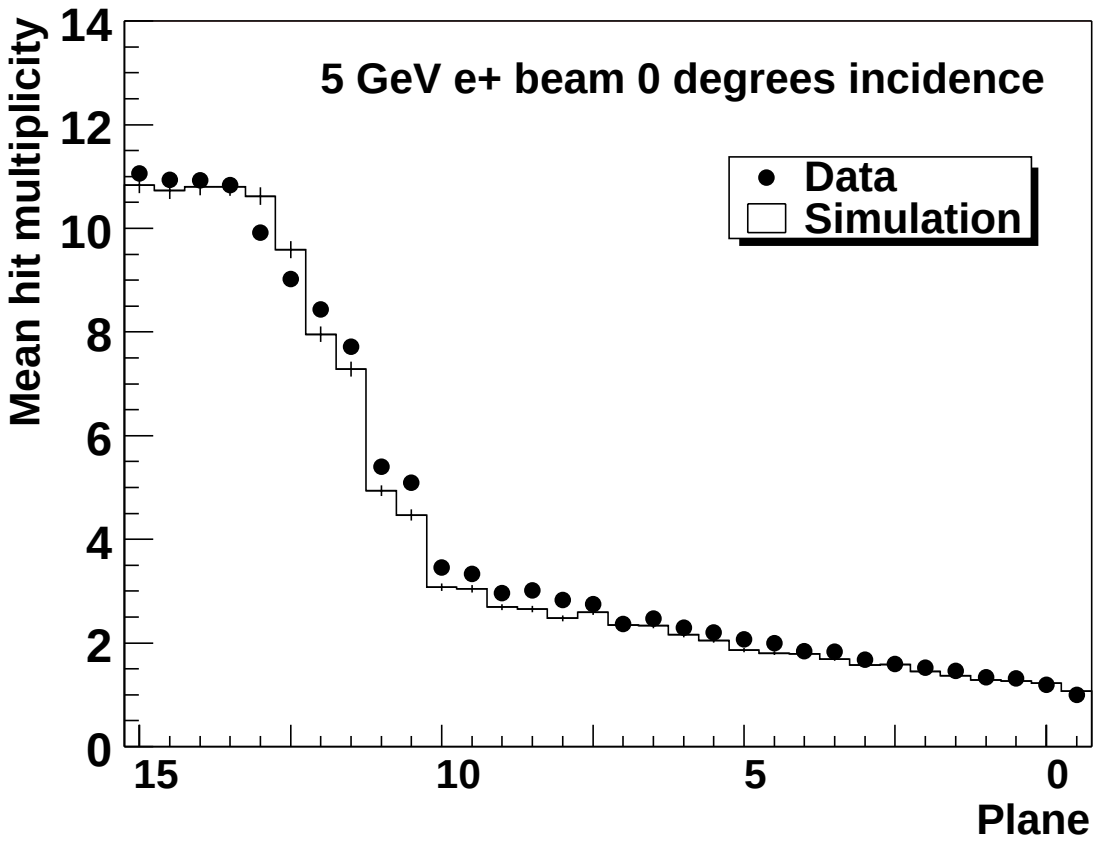

Figure 10: Mean hit multiplicity for all layers for a 5 GeV positron at 0° incidence. Charge sharing correction is applied to the *GLASTSIM* output.

entire detector, which had the highest number of associated clusters. As before, if several tracks had the same number of associated clusters, their chi-squared values were used to make the final selection. Using a standard least squared technique, a new track was fit to all the clusters associated with this best–track. The weight given to a cluster was determined by the number of strips that composed it. This new track was used to calculate the predicted position of the clusters. Once again, the residual of a given cluster was the difference between its predicted position and its measured position. The total offset of either a layer or a ladder is given by the mean of a Gaussian fit to its residual distribution.

Having developed the above procedures, an iterative process was implemented. We began with the two-layer method, as it allowed us to define a coordinate system that did not change from one iteration to the next. Initial gross corrections were made using this method, roughly aligning the detector with respect to a fixed reference point. Two iterations were carried out, the second time using the results of the first as corrections to the position of the layers. The original corrections were as high as 100 μm. The next step invoked the least squared method. Four iterations were performed using this method to correct for layer offsets. Making corrections by layer, we aligned the detector to within approximately 25

μm.

To further improve the alignment the analysis was performed on individual ladders rather than in layers, and the alignment improved by about 35%. Figure 11 shows the residual distribution for all ladders before any corrections were made. Tracks had an average chi-squared value of 1.74 and the detector was aligned to within 60 μm. Figure 12 shows the same

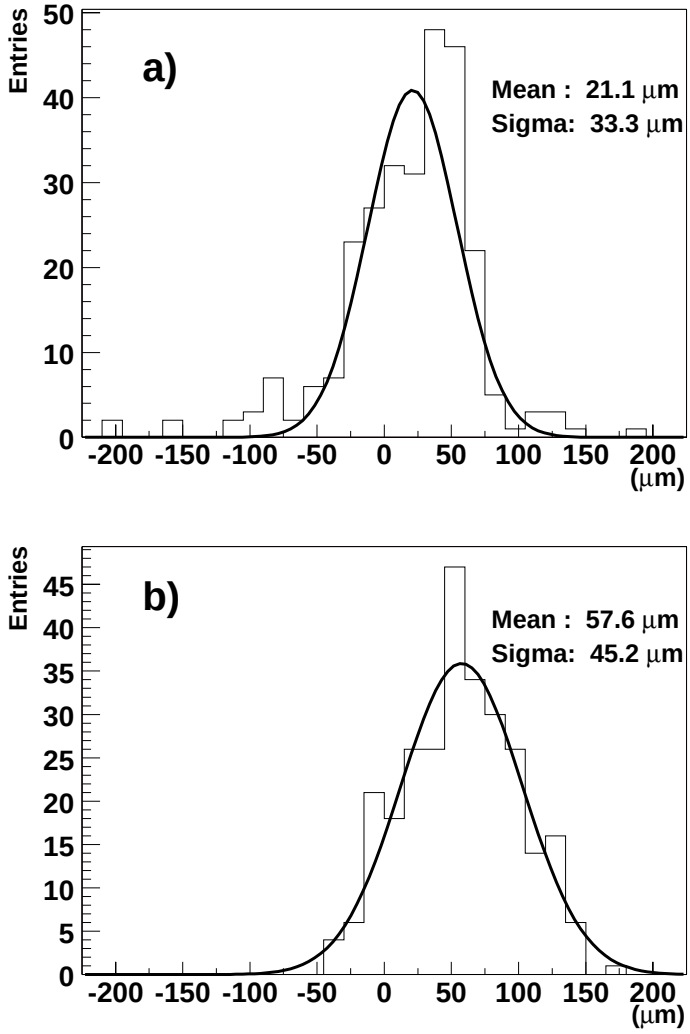

Figure 11: Residuals for all ladders before alignment for the two measured coordinates, a) x and b) y. Results from the Gaussian fit are also shown.

distribution after all the corrections were made. Tracks now have an average chi-squared value of 1.40 and the tracker is aligned to within 18 μm, while the layers are aligned, with respect to each other, to better than 10 μm.

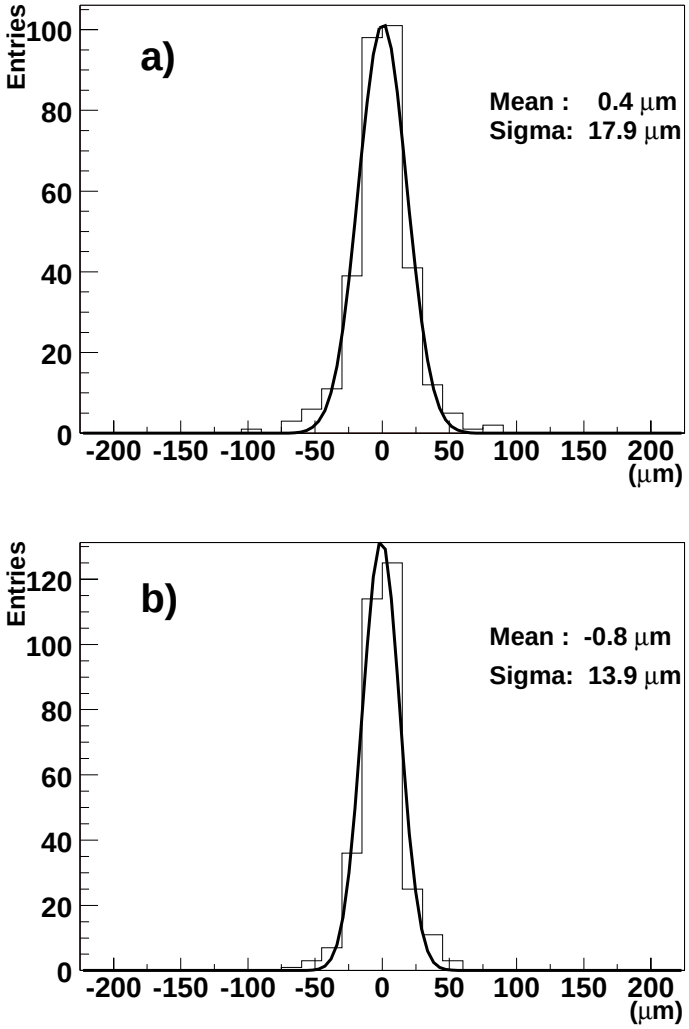

Figure 12: Residuals for all ladders after alignment for the two measured coordinates, a) x and b) y. Results from the Gaussian fit are also shown.

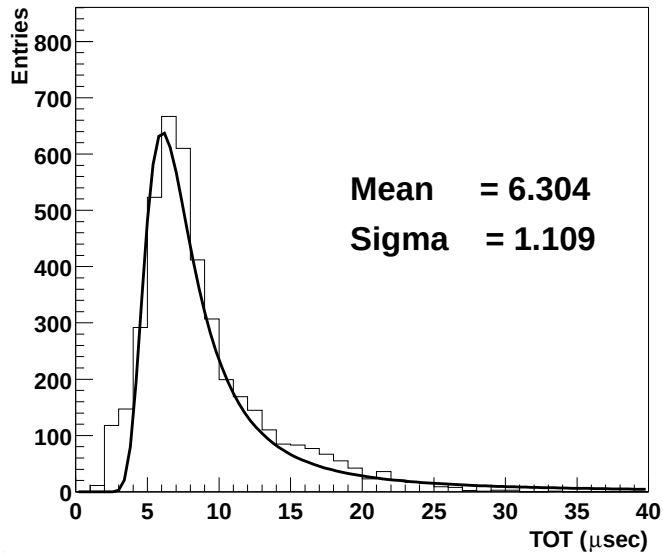

Figure 13: Distribution of TOT values for a 20 GeV positron run with a Landau fit overlaid (1 count = 200 ns).

5.5 Time–over–Threshold

As shown in Fig 1, each layer of the silicon tracker measures only one spatial coordinate. The Time–Over–Threshold (TOT) is calculated by combining all the fast–OR signals in a layer. This gives a crude measurement of the average amount of energy deposited in a single strip for that layer. The TOT measures the amount of time that the charge on any strip in one layer is above a threshold value. First investigations on the TOT can be found in [13]. Throughout the analysis we have found that the TOT can be used to find photon pair conversion points and to improve the charged background rejection.

The TOT is stored as clock counts (1 count = 200 ns). The calibration was performed by injecting charge via an external capacitor into a single amplifier channel and measuring the corresponding width of the fast–OR signal. The response was linear up to 20 mips (1 mip $\simeq$ 7 μs) and for larger input signals, saturation was seen with typical widths of the order of 100 μs.

To obtain the relationship between time and energy deposited in data we analyzed two different positron runs, with beam energies of 2 and 20 GeV. Figure 13 shows the TOT distributions for a typical layer with a Landau fit overlaid. We verified the mean of the distributions for all layers and values fall between 6–7 μs. On average the values from the 20 GeV run are 0.5 μs higher than the values from the 2 GeV run ($\lesssim$ 10% effect). This small difference can be attributed to the fact that at these energies the dE/dx changes logarithmically with the energy. Therefore we use the average value between these two runs as our reference value. Hereafter, we refer to TOT in units of mips.

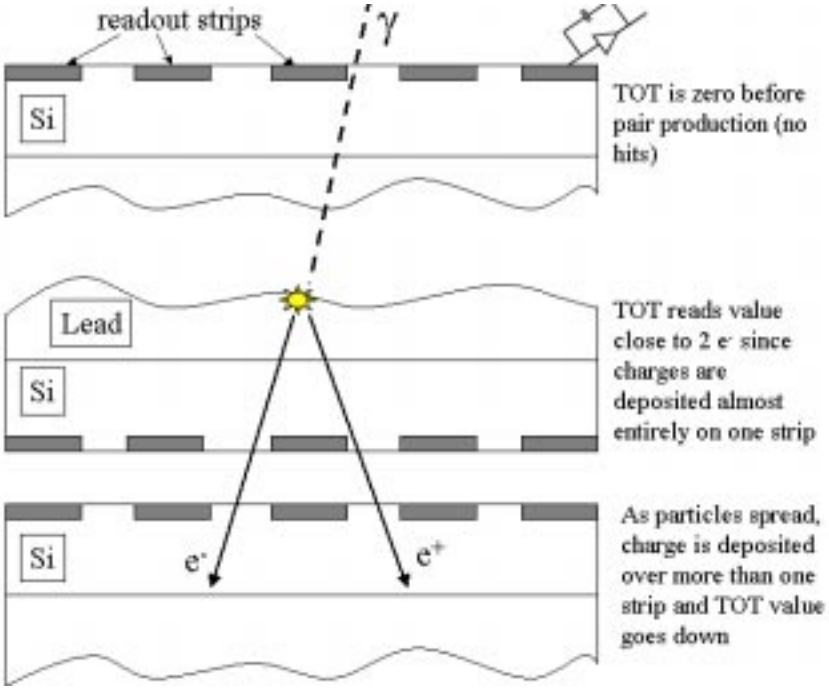

Figure 14: Schematic of a photon conversion. If the silicon layer is close to the conversion point there is a chance that both particles deposit their energy on the same strip.

5.5.1 Vertex finding with the TOT

We investigated the possibility of finding the photon conversion vertices by using the TOT information. The idea is illustrated in Fig 14. When the e^-/e^+ pairs are produced they stay close to each other until they traverse enough material to be spread apart by initial trajectories and multiple scattering. If the silicon planes are very close to the conversion point, and the strip pitch is large, there is a good possibility that both the positron and the electron deposit their energy on the same strip on the silicon layer just after the conversion point. Note that if there are two strips hit in one plane, the TOT value is similar to that of one mip. As these particles move through the tracker their separation increases and they produce hits on more than one strip.

Therefore, immediately after the conversion point we expect the TOT to register a value close to two mips, and as the particles move through the tracker the TOT value should return to one mip. For the silicon layer right above the conversion point the TOT should be zero since at this point no charged tracks have been created. This is what is observed for a normal incidence photon run with beam energy of 20 GeV, and is shown in Fig 15. Figure 15a shows a layer that is right above the conversion point and it should not have registered any hits. The few non zero entries correspond to incorrectly reconstructed events. For the layer located just after the conversion point, the separation between the e^- and the e^+ is small and they frequently hit only one strip, so the TOT registers a value close to 2 mips (Fig 15b). Then as the particles scatter through the tracker they spread their charge

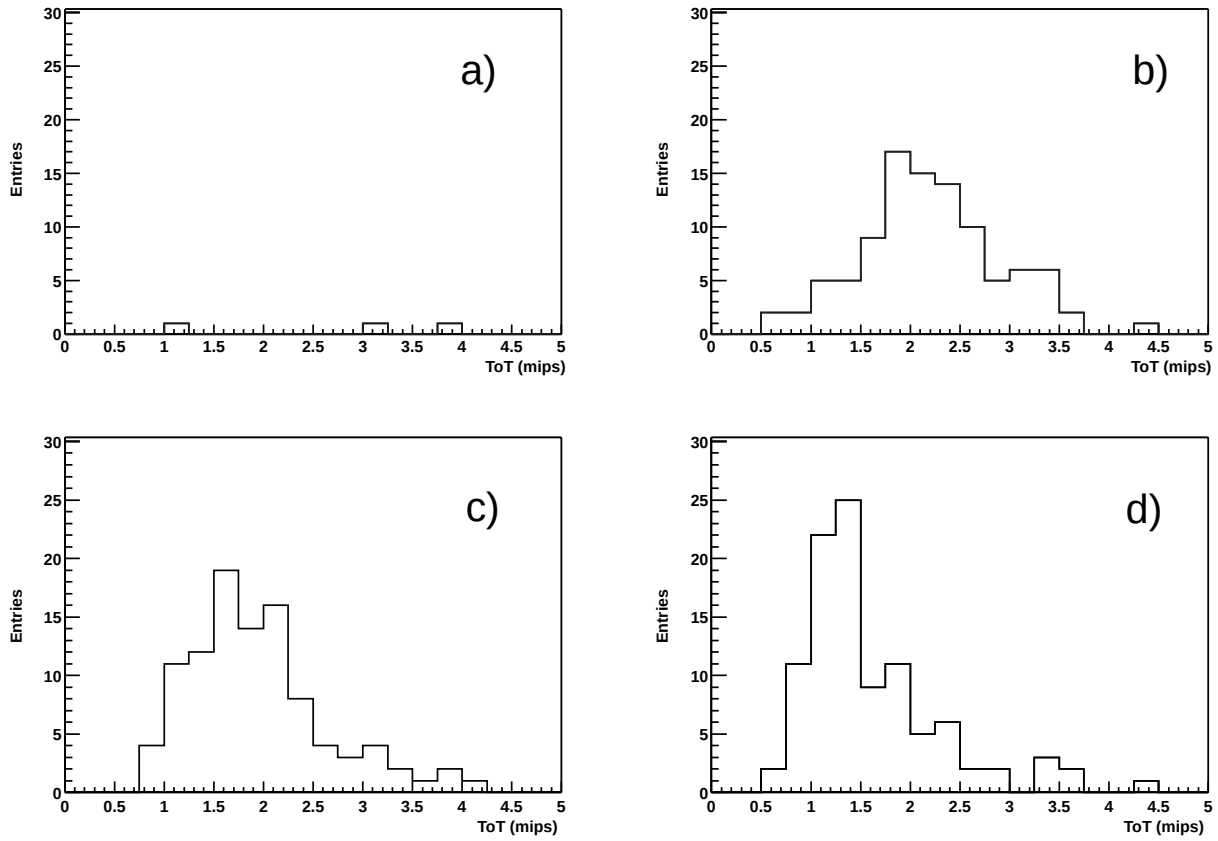

Figure 15: TOT distributions for layer a) above conversion point, b) right below conversion point and c) and d) right below layer shown in b).

over more than one strip and the TOT returns to a value closer to that corresponding to one mip as shown in layers from Fig 15c and Fig 15d . This effect was seen for all layers, so the TOT could be used to locate a conversion in any layer of the tracker, except the topmost where there is no information from the TOT of the layer above.

Figure 16 shows a distribution of TOT values in *one layer* for photons produced from a 20 GeV beam. Events were chosen that either converted three planes above the layer observed (far events), or immediately before the layer observed (near events). The TOT values should correspond to one or two mips, respectively. The filled circles show the distribution of both types of events. The dashed histogram shows the distribution of the far events (one mip candidates). The solid histogram shows the difference between all events and the dashed histogram and corresponds to the near events (two mip candidates). From inspecting with the event display, the two mip candidates that have TOT values $\lesssim 50$ counts, we found three types of events. First, nearly half of these events have hits in two strips in the layer after the conversion point, therefore, the TOT is lower than a value corresponding to two mips since the energy was shared between two strips. Second, the electron and positron can deposit most of their energy onto one strip, but enough can be shared by other strips to

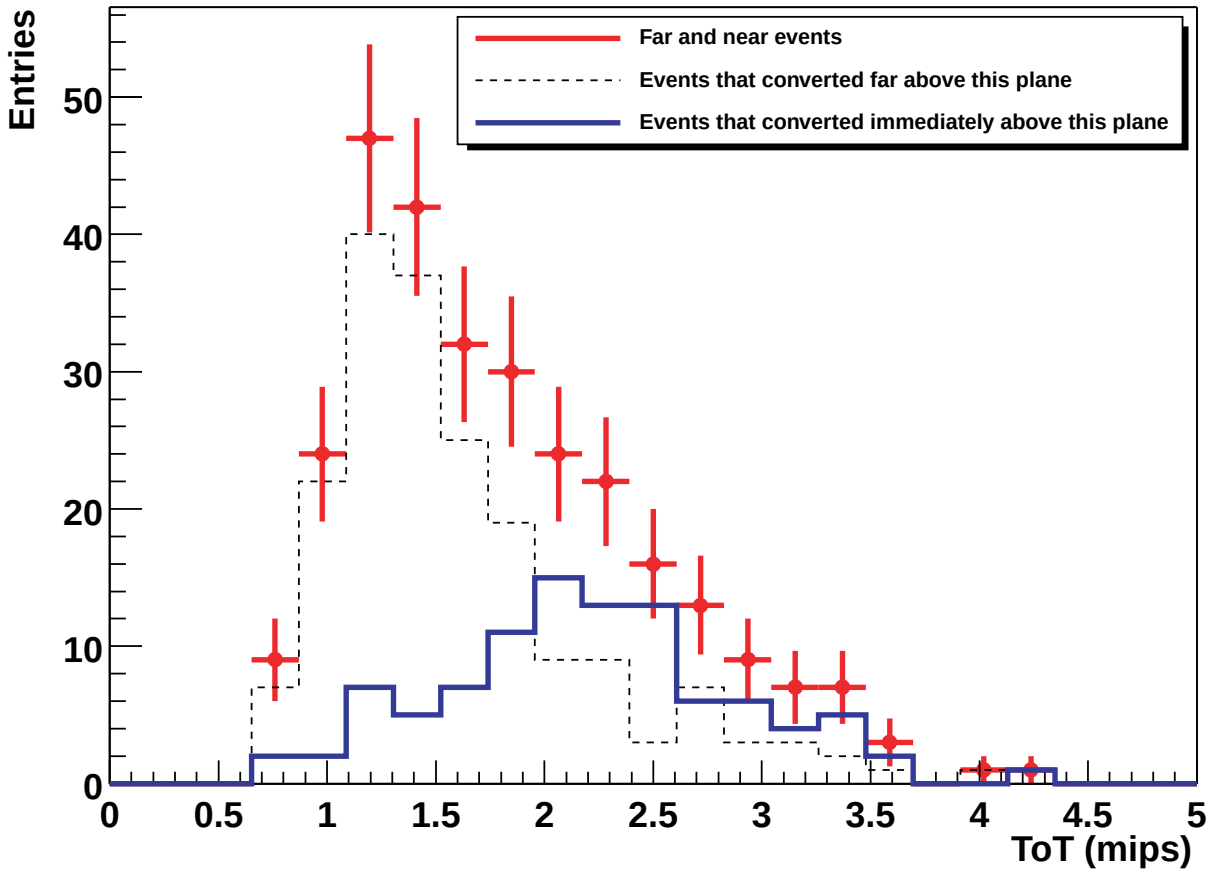

Figure 16: TOT distributions for photon candidates near and far from a given plane.

lower the TOT, but not enough to register a hit. Third, in some events only one of the two particles (electron or positron) register a hit, and the other particle may be missed completely. Therefore, with improvements in the algorithm we can still increase the significance of the separation between both types of events.

5.6 Point Spread Function (PSF)

The point spread function, which is energy dependent, describes the difference between reconstructed and true direction of incident gamma rays projected onto the celestial sphere. It is commonly characterized by the 68% space containment angle (PSF68), and the 95% space containment angle (PSF95), which indicate the radius of a circle which contains in an area 68% and 95% of the events, respectively. The fact that the tracker is also a converter imposes limitations on its performance. A particle deviates from its original trajectory either due to multiple scattering or due to the energy lost in the tracker. As mentioned before, to provide an optimal solution to track fitting, the reconstruction uses the Kalman filter technique [14]. Misidentification of the photon conversion vertex or initial directions of the positron and electron will result in a wrong reconstructed photon direction and consequently

a degraded PSF. The pattern recognition algorithm uses all combinations between any silicon hit and the centroid of the position of the calorimeter cluster as seeds for the photon conversion. It searches for two tracks that share a common vertex or an initial segment, and inverted "V" topology is a clear indication of a photon conversion into a positron and electron. The candidate with the longest and most straight tracks with no hits in the silicon plane immediately above the vertex is selected as the main photon candidate in the event. The pattern recognition uses the Kalman filter to extrapolate the tracks and their covariant matrices back and forward around the track to search for hits. The pattern recognition algorithm assigns silicon hits to both tracks simultaneously, so that they can compete for hits in a given plane, thereby resolving the xy ambiguities in a plane whenever possible. The track reconstruction efficiency has been estimated using *GLASTSIM* to be better than 90% for all triggers with a vertex reconstruction efficiency of approximately 80%. These remain unchanged as the energy of the incoming photon varies from 100 MeV up to 10 GeV and with incident angles up to 60°. Due to the design of the tracker (see 2.2), the point spread functions for the front and back section have been studied separately.

To select photons with well reconstructed directions we rejected events

- with calorimeter energy below 10MeV,
- with the reconstructed photon vertex in or vertically aligned with the uninstrumented area of the detector,
- with clusters containing noisy strips ($> 0.1\%$ occupancy),
- where the first plane hit in the reconstructed photon was the first plane in the tracker (upstream the beam),
- where other tracks where reconstructed above the main photon,
- and without good correlation between the energy as measured by the calorimeter and by the tagger.

After the selection above one finds the true incident angle of the incoming Beam in the coordinate system of the tracker. The incoming direction is the average of all reconstructed photon directions in both x and y projections. The divergence of the beams were found to be negligible (< 0.1 mrad). The direction of the individual photons was found from the scalar product of the reconstructed photons with the incident angle. Since the PSF68 and the PSF95 are energy dependent, the energy determination of individual photons plays an important role. Systematic uncertainties in the energy measurement from our reconstruction program have been studied using the Monte Carlo simulation by halving the total light output in the calorimeter and determining its effect on the PSF. For the test beam data an additional uncertainty exists since we do not know what the true value of the photon energy is. Therefore for each data point we averaged the energies measured by the photon tagger and by the calorimeter. The error on this average has been estimated to be 12% based on the knowledge of the correlation between both energies in our selection criteria.

At this point an additional correction is still needed. Most of the data was obtained from a radiator in the beam line with 2.7% radiation lengths, which introduces a significant intrinsic spread in the incident photon direction. The probability that two photons are created in the radiator is about 20%. While only about 60% of these photons convert in the tracker, all are measured in the calorimeter. This can lead to a mis-assignment of the energy, if one of the more numerous low-energy photons converts but the energy of a high energy photon is measured. Data from few dedicated runs were used to correct for this effect. We calculated the PSF68 for three radiator thickness and extrapolated it to zero thickness. Figure 17 shows the dependence of the PSF at 0° for 3.5 GeV (squares) and 5 GeV (circles) photons for different radiator thickness. One clearly sees that the PSF is degraded by the presence of thick radiators that increase the probability of having multiple photons. From Fig 17 we estimate the corrections from 2.7% to 0% radiator for 3.5 GeV and 5.0 GeV to be of the order of 30% and 40%, respectively. To verify that we used an analytical model that took into account multiple radiation in the converter foil and the energy dependence of the point spread function for the BTEM. This correction is larger for high energy photons and we estimated to be about 10% at lower energies (<0.9 GeV).

This correction on the PSF is not only crucial for this analysis but carries an uncertainty of about 15% and dominates all systematic effects. Figure 18 shows the PSF at 0° incident angle for 68% containment radius as a function of the reconstructed energy for both front (circles) and back (squares) section of the tracker, for data (filled symbols) and Monte Carlo simulation (open symbols).

The expected 1/E behavior is clearly seen. As the photon energy increases, multiple scattering becomes less important and the point spread function decreases. At high energies the point spread function is dominated by the finite spatial resolution of the silicon detectors ($\simeq 60$ μm). The thick radiators on the back of the tracker degrade the point spread function by slightly more than a factor of 2.

6 Conclusion

For the SLAC 1999/2000 beam test the GLAST collaboration built the Beam Test Engineering Model (BTEM) whose overall size is close to that of one of the modules of the full GLAST instrument. Note that not all features of the flight design have been incorporated yet. We have demonstrated the feasibility of an integrated data acquisition scheme with self–triggering scheme and developed a data processing scheme that uses a file format that adheres to the object–oriented paradigm thereby reducing the complexity of reading and writing event data. We have also proven that low energy neutrons interacting in the hydrogen within the plastic scintillator of the ACD, are not a significant source of backsplash false signals. We have developed a method to improve the energy resolution in the calorimeter, which uses the correlation between the escaping energy and the energy deposited in the last layer of the calorimeter. We have used the hadron beam to align the silicon tracker ladders in a plane to within 18 μm. We have further improved our Monte Carlo simulations and validated the distribution of number of hits in the tracker (front and back sections) for on–axis and off-axis incidence. This is very important since the energy lost in the tracker can

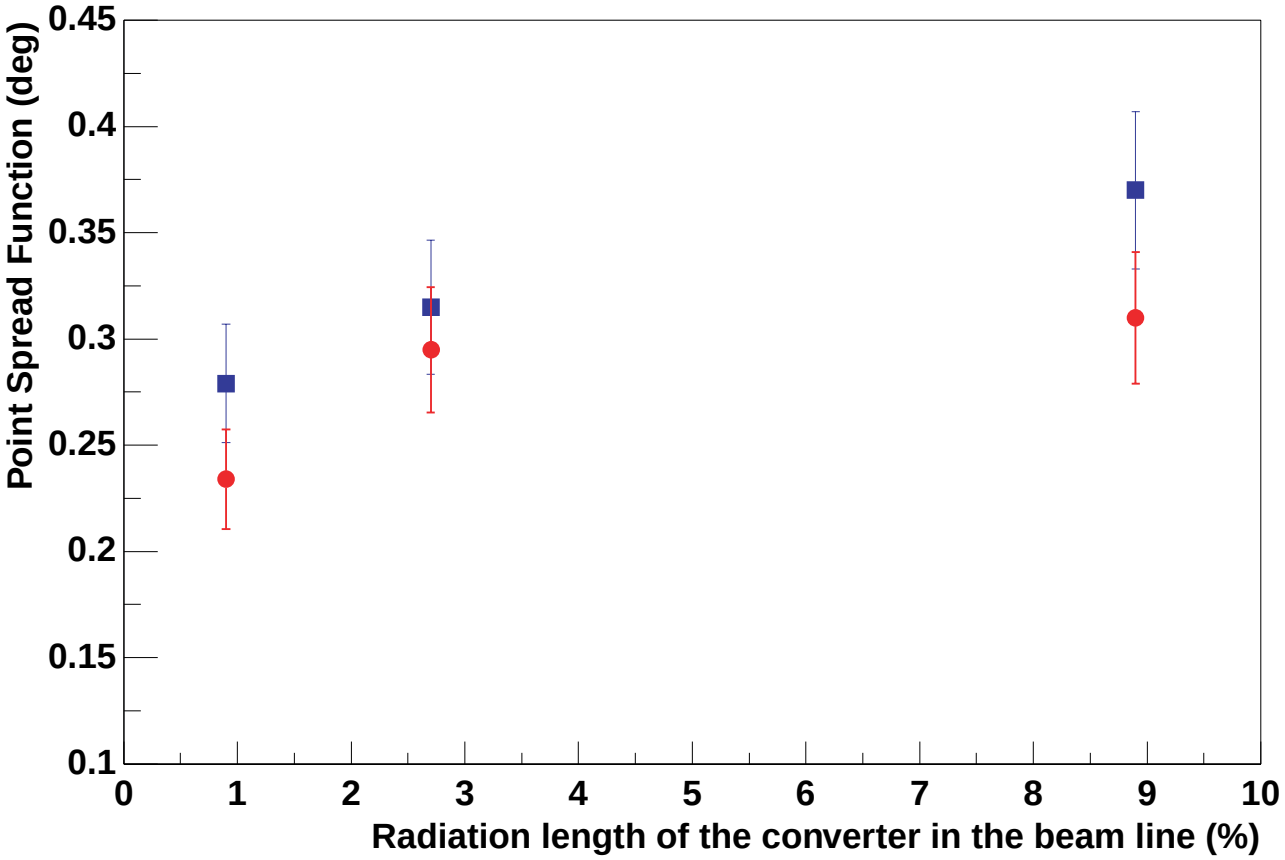

Figure 17: PSF at 0° incident angle for 68% containment for three different radiators for 3.5 GeV (squares) and 5 GeV (circles) photons in the data.

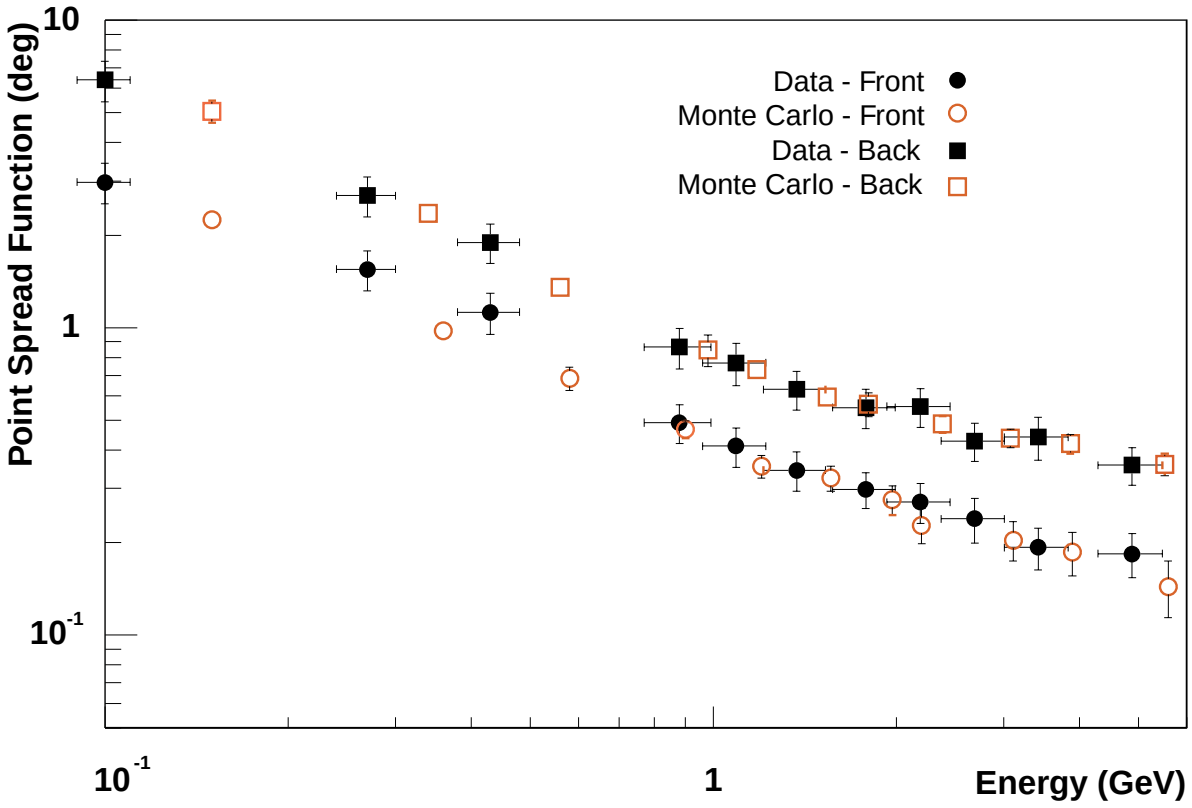

Figure 18: PSF at 0° incident angle for 68% containment radius as a function of the reconstructed energy for both front and back sections of the tracker. Data points have been corrected for the thickness of the radiator in the beam line (see text).

be estimated from the total number of hits. We have shown that the Time–over–Threshold from the tracker is a promising tool as a photon conversion finder and can be used as an additional handle on the charged background rejection. We have also measured the point spread function for both sections of the tracker. For normal incidence and 68% containment the results between Monte Carlo and data agree well for photon energies from 100 MeV up to 5 GeV. Among the most important achievements of this beam test has been to complete a full tower system integration, further developing our data processing path and to validate the performance of the back section of the tracker. We have also acquired invaluable experience towards the construction of the full scale flight instrument.

7 Acknowledgements

We thank M. Kuss for comments to this paper. We are indebted to all the technicians who made this experiment possible. Special thanks to the SLAC Experimental Facilities Department and Machine Operations Group for their extraordinary help. We also acknowledge the SLAC directorate for their strong support.

References

[1] P. Michelson *et al.*, Proc. SPIE, Vol **2806** (1996) 31.

[2] D.J. Thompson *et al.*, ApJ. Suppl. Vol **86** (1993) 629.

[3] W. Atwood *et al.*, Nucl. Inst. and Meth. **A446** (2000) 444.

[4] V. Chen *et al.*, *The Readout Electronics for the GLAST Silicon–Strip Pair–Conversion Tracker*. Proceedings of the 4^{th} International Symposium on Development and Application of Semiconductor Tracking Detectors, March 20–25 2000, Hiroshima, Japan.

[5] E. Atwood *et al.*, *The Silicon Tracker of the Beam Test Engineering Model of the GLAST Large Area Telescope*, SLAC–PUB–8466, June 2000. Accepted for publication in Nucl. Inst. and Meth. **A**.

[6] P. Allport *et al.*, *The Assembly of Silicon Tracker of the Beam Test Engineering Model of the GLAST Large Area Telescope*, SLAC–PUB–8471, June 2000. Proceedings of the 4^{th} International Symposium on Development and Application of Semiconductor Tracking Detectors, March 20-25 2000, Hiroshima, Japan.

[7] R. Brun and F. Rademakers, Nucl. Inst. and Meth. **A389** (1997) 81-86. See also http://root.cern.ch/

[8] R. Brun and D. Lienart, *HBOOK User Gudie: CERN Computer Center Program LIbrary. Long Write Up. Version 4*, CERN Y-250, (1987).

[9] A. Moiseev and J. Ormes, paper in preparation.

[10] W. P. Swanson, *Radiological safety aspects of the operation of electron linear accelerator*, International Atomic Energy Agency Technical Report Series **188** (1979) 87.

[11] W. B. Atwood *et al.*, Int'l J. Modern Physics **C**, Vol 3 (1993), 459.
T.H. Burnett *GISMO: An object–oriented approach to particle transport and detector modeling* . Proceedings of the International Conference of Monte Carlo Simulation in High Energy and Nuclear Physics, Tallahassee, Florida 22-26 February, 1993.

[12] W. R. Nelson *et al.*, *The EGS4 Code System*, SLAC Report No. 265, Stanford CA. 1985

[13] M. Nikolaou, *Simulation and Analysis of the GLAST Beam Test Engineering Model*, Royal Institute of Technology, Stockholm, TRITA–FYS-9107, 2000. Master Thesis.

[14] P. Billoir, Nucl. Inst. and Meth. **A 225**, (1984) 352 and references therein.